Materials Science in Semiconductor Processing 146 (2022) 106700

Contents lists available at ScienceDirect

Materials Science in Semiconductor Processing

journal homepage: www.elsevier.com/locate/mssp

Preparation and study of ammonia gas sensor based on ZnO/CuO heterojunction with high performance at room temperature

Cao Cheng [a], Chu Chen [a], Hongyan Zhang [a,*], Yong Zhang [b,**]

[a] Xinjiang Key Laboratory of Solid State Physics and Devices, Xinjiang University, Urumqi, 830046, PR China
[b] Electrical and Computer Engineering Department, The University of North Carolina at Charlotte, NC, 28223, USA

ARTICLE INFO

Keywords:
Gas sensor
NH_3
ZnO/CuO
Heterojunction
First principles

ABSTRACT

An ammonia (NH_3) gas sensor based on ZnO/CuO (ZC) heterojunction was prepared by hydrothermal method and the sensing mechanism was studied by first principle calculations based on density function theory (DFT). Experiments show that NH_3 sensor based on ZC heterojunction has low detection limit (0.39 ppm), fast response/recovery time (2.3 s/2.1 s), high sensitivity, good selectivity, strong stability and high humidity resistance at room temperature (RT). Compared with ZnO, ZC has more oxygen free radicals appeared on surface of heterojunction, and has redox reactions with NH_3 molecules to release more electrons to improve sensitivity of ZC. Calculations show that excellent performance is mainly due to the strong adsorption energy of ZC heterojunction to NH_3 detection. The polarity of NH_3 molecules is enhanced under strong built-in electric field formed by ZC heterojunction which absorbs more NH_3 molecules to react with oxygen radicals on surface of ZC and induce high response of ZC to NH_3 molecules. This study indicates that ZC heterojunction structure can effectively improve ZnO sensors for NH_3 detection at RT, which is helpful for application of metal oxide semiconductor.

1. Introduction

As a colorless toxic gas, ammonia (NH_3) is widely existed in agriculture, industry and people lives. For the Occupational Safety and Health Administration (OSHA), it will pollute atmosphere and harm people's health when concentration of NH_3 exceeds the threshold value of 25 ppm in environment [1–3]. In general, the pungent odor of NH_3 is an early reliable warning signal of harmful concentrations, but it is difficult to detect NH_3 in time due to people suffering from olfactory fatigue in low concentration of NH_3 for long time [2,3]. So, it is play an important role for early monitoring in environment to develop an NH_3 sensor of high sensitivity and low detection limit.

There are many kinds of gas sensors, including the type of surface acoustic wave (SAW), resistive semiconductor, capacitive, quartz vibrator and metal oxide semiconductor diode capacitor voltage, etc. [4–7]. Among them, resistive semiconductor gas sensor has the advantages of high efficiency, low consumption, fast response speed, easy to carry and so on, and it is the most valuable gas sensor in research and application [8–11]. Metal oxide semiconductor is one of the commonly used materials for resistive semiconductor gas sensor, because it has excellent gas sensitive performance, wide detection range, simple preparation and low cost [2,8]. Most metal oxide semiconductor gas sensors have good sensing performance only at high operating temperature, but high work temperature will affect the service life of the sensor, work efficiency and limit the type of gas to be detected [3,8]. It is urged to develop a high sensitivity gas sensor for room temperature (RT, 25 °C).

As a n-type metal oxide semiconductor with wide bandgap, ZnO is considered to the most promising gas sensitive materials, because the good electromagnetic properties, high carrier mobility, strong physical, and chemical stability [8,9]. Due to its high operating temperature requirements, low sensitivity, poor selectivity and long response/recovery time, practical application of the sensors based on ZnO is hindered [10–12]. It has been reported that the formation of heterostructure between different metal oxide semiconductor can improve the gas sensitivity of sensors at RT [13]. The heterojunction introduces a thick electron depletion layer between two different metal oxide semiconductor materials, which increases resistance of the sensor. Furthermore, oxygen molecules in the air can capture electrons on surface of heterojunction to form a large number of oxygen radicals. The

* Corresponding author.
** Corresponding author.
E-mail addresses: zhanghyxj@163.com (H. Zhang), yong.zhang@uncc.edu (Y. Zhang).

https://doi.org/10.1016/j.mssp.2022.106700
Received 19 December 2021; Received in revised form 24 March 2022; Accepted 4 April 2022
Available online 11 April 2022
1369-8001/© 2022 Elsevier Ltd. All rights reserved.

heterojunction is destroyed and the thickness of electron depletion layer is reduced when target gas redox reacts with oxygen radicals on its surface to release electrons to heterojunction, which is accompanied by orders of magnitude change in resistance value [14].

As a p-type metal oxide semiconductor with narrow bandgap, CuO has broadly used for p-n heterojunction gas sensors, because the abnormal electromagnetic activity and stable physical and chemical properties. Liang et al. prepared a ZnO/In_2O_3 heterojunction NO_2 sensor with good sensitivity at RT [13]. Sharma et al. prepared an n-MoS_2/p-CuO heterojunction NH_3 sensor with excellent performance at RT [15]. Hu et al. studied a ZnO–CuO heterojunction high-performance ethanol sensor and explained the related oxygen adsorption, tunneling effect and p-n heterojunction [16]. Yu et al. developed a ZnO–CuO heterojunction ethanol sensor, and the results showed that the composite between materials enhanced the sensor's response to ethanol [17]. Up to now, there are few reports on the detection of NH_3 at RT based on ZnO/CuO (ZC) heterojunctioned high performance sensor.

In this work, ZC heterojunction was prepared by hydrothermal method to be used for NH_3 detection. Experiments show that ZC heterojunction can effectively improve selectivity, sensitivity and response/recovery time, detection limit and stability of ZnO when it is used for NH_3 detection at RT. Gas sensing mechanism was studied by density functional theory (DFT), and formation of heterojunction enhances adsorption energy to NH_3 molecules. It is helpful for the gas sensor to capture more NH_3 molecules and there are more redox reactions with oxygen radicals on its surface, so as to improve sensing performance. This study indicates that ZC is an ideal gas sensing material for NH_3 detection, which is expected to solve the problems of poor sensitivity and low response of electrical gas sensor at RT.

2. Experiments

2.1. Materials and characterizations

Zinc acetate ($Zn(CH_3COO)_2$), copper acetate ($Cu(CH_3COO)_2{\cdot}H_2O$), potassium hydroxide (KOH) and ethanol (C_2H_6O) were purchased from Sangon Biotech (China, www.sangon.com). Lithium chloride (LiCl), magnesium chloride ($MgCl_2$), potassium carbonate (K_2CO_3), sodium bromide (NaBr), sodium chloride (NaCl) and potassium chloride (KCl) were also purchased from Sangon Biotech. All reagents were analytical grade (AR) and can be used directly without further purification. Deionized water was used as test reagent in experiments. Furthermore, the purity of each liquid used in the process of gas configuration is hydrogen peroxide (H_2O_2, (30%)), ethanol (C_2H_6O, (≥99.7%)), acetone (C_3H_6O, (≥99.5%)), formaldehyde (HCHO, (37.0%–40.0%)), NH_3 (25.0%–28.0%).

Crystal structure of the samples was determined by X-ray powder diffractometer (XRD, Advanced 8, Germany) under Cu-Kα radiation with scanning interval of 5–80° and operating voltage of 40 kV. Field emission scanning electron microscopy (SEM, S-4800, Hitachi, Japan) was used to determine surface morphology. Distribution of elements in the crystal was measured by an energy dispersive X-ray spectrometer (EDX) that was attached to SEM. Morphology and lattice of the sample were determined by transmission electron microscopy (TEM, JEOL JEM-2100F, Hitachi, Japan). Surface area and pore size distribution of the material were evaluated using Brunauer-Emmett-Teller (BET, Micromeritics ASAP 2460, US). UV–Vis absorption spectrum was measured by UV–Vis (PerkinElmer, Lambda 650, US), and bandgap of the sample was estimated. Valence states of ions was measured by X-ray photoelectron spectroscopy (XPS, Thermo Fisher Scientific, US) with monochromatic Al Kα radiation as excitation source. Chemical composition was studied by Fourier transform infrared (FTIR, Bruker-Vertex 70, Karlsruhe, Germany) spectrometer. Electrical performances of the sample were tested by electrochemical workstation (ZAHNER, Germany) at 1 V.

2.2. Preparation of CuO

CuO was synthesized by hydrothermal method. 0.54 g Cu $(CH_3COO)_2{\cdot}H_2O$ and 1.40 g KOH were dissolved in 50 ml deionized water and magnetically stirred for 10 min to form a clear solution. The obtained mixed solution was transferred into a 100 ml polytetrafluoroethylene autoclave and kept at 100 °C for 10 h. After being cooled down to RT, the reaction product was centrifuged and washed several times at 8000 rpm by alcohol and deionized water. Then the precipitate was dried at 60 °C for 24 h to obtain CuO sample.

2.3. Preparation of ZnO and ZC

ZnO and ZnO/CuO were synthesized by one-step hydrothermal method. Firstly, 0.55 g of $Zn(CH_3COO)_2$ and 1.40 g of KOH were dissolved in 50 ml deionized water and magnetically stirred for 10 min to form clear solution. Then, 0 g, 0.15 g (30%), 0.25 g (50%) and 0.35 g (70%) $Cu(CH_3COO)_2{\cdot}H_2O$ were separately added to the above solution, and magnetically stirred for 30 min. The obtained mixed solution was transferred into a 100 ml polytetrafluoroethylene autoclave and heated at 100 °C for 10 h. After the reaction products were cooled down to RT, the samples were centrifugally washed several times with ethanol and deionized water at 8000 rpm. Finally, the products were dried at 60 °C for 24 h to get ZnO, ZC1, ZC2 and ZC3 samples.

2.4. Sensor tests

Appropriate amount of sample and deionized water were put into agate mortar with a ratio of 1:4 to be stirred for 3 min. The stirred sample was coated on Ag–Pd cross electrode with wool brush, and the coated electrodes were placed in a dried oven at 60 °C for 1 h. Then the prepared electrodes were placed in the air at RT for 48 h to be aged. Finally, the sensing performance was tested by electrochemical workstation at RT with voltage set to be 1 V. Here, the alumina ceramic Ag–Pd cross electrode used in the experiment has an overall dimension of 13.4 × 7 × 0.635 (mm^3), the line width and spacing are 0.2 mm. Fig. 1 shows the schematic diagram and process of the experiments.

In the process of sensor testing, all gases are generated by thermal evaporation, and the concentration calculation formula is $Q = 10^{-9} \times (C \times M \times V)/(d \times 22.4 \times \rho) \times (T_A + 273)/(T_G + 273)$ [18]. Where Q, d and ρ is the volume, purity and density of the liquid to be taken, V, T_A and T_G are the volume of the experimental cylinder, ambient temperature and container temperature. C and M are the concentration and molecular weight of the target gas to be prepared, respectively. Response of the sensor is defined as $R=(I_g\text{-}I_a)/I_a = \Delta I/I_a$, where I_a and I_g represent the current values of the sensor in air and target gas respectively.

The saturated salt solutions of LiCl, $MgCl_2$, K_2CO_3, NaBr, NaCl and KCl were prepared in a relative humidity (RH) environment of 11%–85%, and tested in a closed condition at RT. During the transition from low to high humidity, the sensor is exposed in the air (30% RH) for about 1 s. Moreover, the time required for the current to reach the equilibrium state is about 3 s. The response degree is calculated by using the real-time response current value, and this is defined as $R=(I_r\text{-}I_b)/I_b = \Delta I/I_b$, where, I_r and I_b are the current values of the sensor under the environmental conditions of 11%–85% RH and air humidity respectively.

3. Results and discussions

3.1. Characterization

In Fig. 2(a), structure and crystallinity of CuO, ZnO, ZC1, ZC2 or ZC3 sample were studied by XRD. Diffraction peaks (2θ) at 31.89°, 34.53°, 36.36°, 47.63°, 56.68°, 62.94°, 68.03° and 69.17° correspond to (100), (002), (101), (102), (110), (103), (112) and (201) crystal planes of hexagonal wurtzite ZnO (JCPDS No. 70–2551). Diffraction peaks (2θ) at

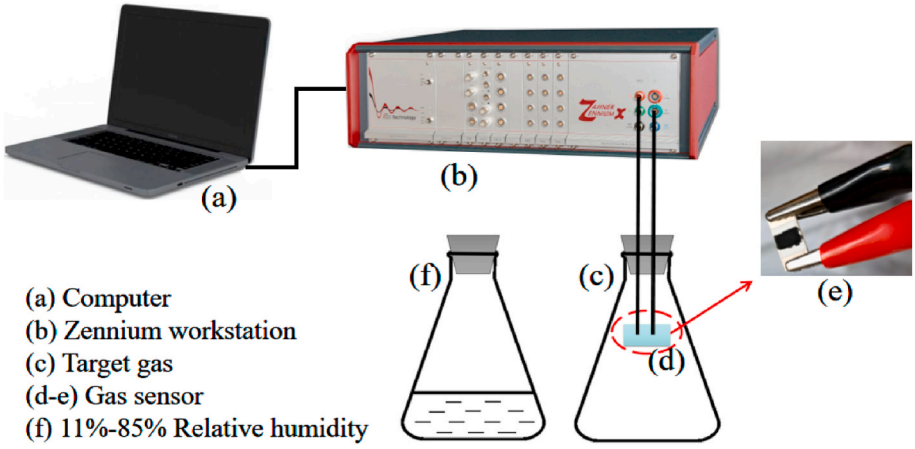

Fig. 1. Schematic diagram of the experiments.

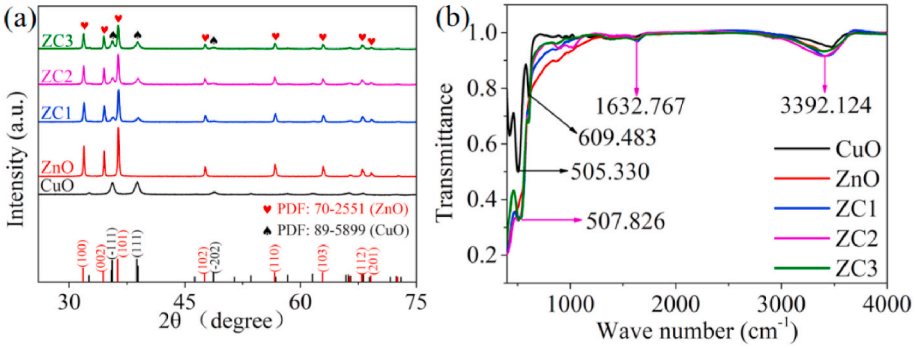

Fig. 2. (a) XRD patterns of CuO, ZnO, ZC1, ZC2 and ZC3, (b) FTIR spectra of CuO, ZnO, ZC1, ZC2 and ZC3.

35.63°, 38.88° and 48.87° correspond to (−111), (111) and (−202) crystal planes of monoclinic CuO (JCPDS No. 89–5899), respectively. No other impurity diffraction peaks are found in all XRD spectra, indicating that ZnO and CuO are successfully prepared. The intensity of ZnO diffraction peak in ZC sample gradually decreases with the ratio of CuO to ZnO. Diffraction peaks of ZnO, CuO and ZC are sharp, which indicates that the crystallinities of ZnO, CuO and ZC are good [19–21].

Fig. 2(b) shows the FTIR spectra of CuO, ZnO, ZC1, ZC2 and ZC3 samples. Peaks at 505.330 cm^{-1}, 507.826 cm^{-1} and 609.483 cm^{-1} correspond to tensile vibrations of Cu–O in CuO, ZC1, ZC2 and ZC3, respectively [21]. The peak at 1632.767 cm^{-1} corresponds to bending vibration of –OH on surface of CuO, ZnO, ZC1, ZC2 and ZC3. In addition, the broad peak at 3392.124 cm^{-1} is attributed to symmetric and asymmetric stretching modes of O–H bond, which can adjust surface

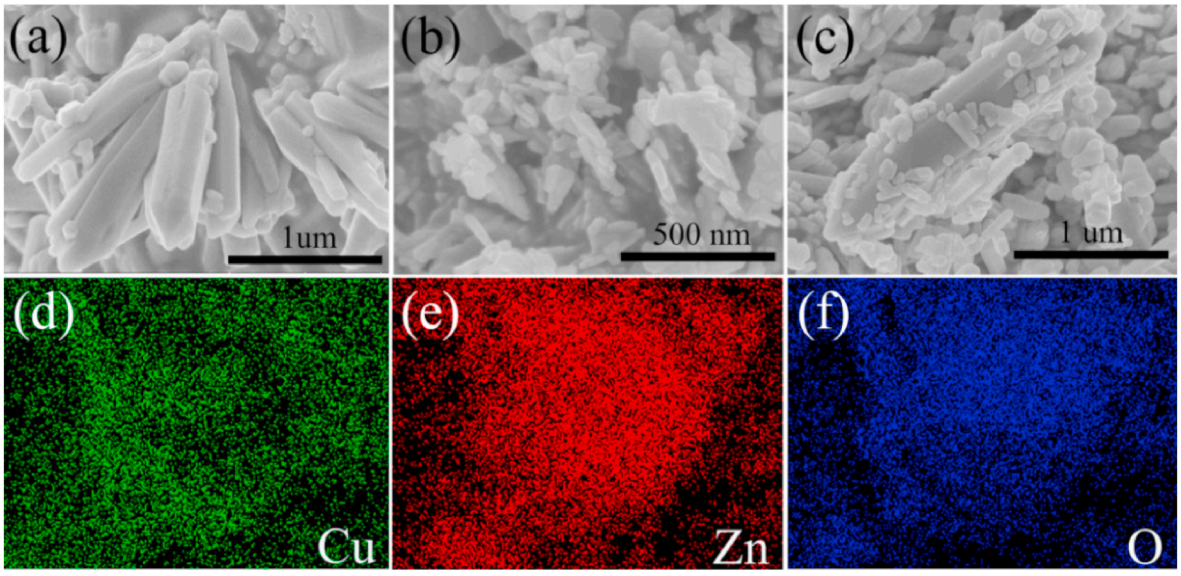

Fig. 3. (a–c) SEM images of ZnO, CuO and ZC2, (d–f) EDS element mapping (Cu, Zn and O) of ZC2 sample.

defects and is conducive to improve gas sensitive performance of the sensor [3]. Compared with CuO and ZnO, surface functional groups on ZC1, ZC2 and ZC3 have slight changes.

Morphology and elemental distribution of ZnO, CuO and ZC2 were carried out by SEM and EDS element mapping, respectively. In Fig. 3(a), ZnO is composed of nanorods with a diameter of about 90 nm and a length of about 1 μm. The CuO sheet in Fig. 3(b) is condensed from nanoparticles with a diameter of about 40 nm. The ZC2 heterojunction material in Fig. 3(c) is formed by adhering CuO to the ZnO surface. The surface of ZnO becomes extremely rough, which can provide more surface active sites for the adsorption of oxygen molecules and target gas molecules [1]. In order to explore spatial distribution of elements in ZC2 material, element mapping was carried out as shown in Fig. 3(d–f). Cu, Zn and O elements are uniformly distributed on surface of ZC2 sample. Fig. 3(d–f) shows the spatial element mapping of Cu, Zn and O, indicating that they are evenly distributed in ZC2 material.

Microstructure of ZC2 was studied by TEM and HRTEM. It can be seen from the morphology of corresponding ZnO and CuO in Fig. 3(a–b) and Fig. 4(a), CuO slice is attached to the ZnO nanorods surface which is similar to Fig. 3(c). In Fig. 4(b–e), lattice spacings are 0.20 and 0.29 nm, that is corresponds to (102) and (100) crystal planes of hexagonal wurtzite structure of ZnO [2], and the lattice spacing of 0.24 nm is consistent with (111) crystal plane of monoclinic structure of CuO [19]. Moreover, a clear boundary between ZnO and CuO lattice stripes with good interface contact can be found in Fig. 4(b), which indicates the formation of p-n heterojunction between CuO nanoparticles and ZnO nanorods. Fourier transformations (FFT) of ZnO and CuO corresponding to HRTEM images of the selected area of ZC2 are in insets in Fig. 4(b) [20]. ZnO and CuO are single crystals with good crystallinity, which is consistent with XRD results as in Fig. 2(a). Fig. 4(f) is the selected area electron diffraction (SAED) corresponding to the blue dotted box region in Fig. 4(b). Diffraction ring in SAED indicates that ZC2 heterojunction is polycrystalline with high crystallinity, this is conducive to the improvement of gas sensitivity [20].

Fig. 5(a–d) shows N_2 adsorption-desorption isotherms, BET specific surface area and corresponding BJH pore size distribution curves of ZnO, CuO and ZC2 materials respectively. Fig. 5(a–c) shows isotherms of ZnO, CuO and ZC2 are basically the same which belong to type IV, and the obvious hysteresis loop is belonging to type H3 [13,20]. In Fig. 5(d), from the pore size distribution, the average pore sizes of ZnO, CuO and ZC2 are about 73.56, 67.94 and 194.15 nm, respectively. Macroporous structure is more conducive to gas diffusion and reaction. The relative BET surface areas for ZnO, CuO and ZC2 are calculated to be 5.14, 33.89 and 7.81 m^2/g respectively. Compared to ZnO, ZC2 composite has a larger specific surface area, which can provide more active sites for the adsorption of gas molecules.

Fig. 6(a–b) describes UV–Vis absorption spectra and Tauc plots of CuO, ZnO, ZC1, ZC2 and ZC3. Absorption peaks of ZnO, ZC1, ZC2 and ZC3 samples appear around 350 nm, which is related to exciton absorption in ZnO, as shown in Fig. 6(a). It is obvious that absorbance of ZC1, ZC2 and ZC3 in the range from 400 to 760 nm is enhanced significantly with the increase of CuO content. And absorption edge of ZnO shifts to visible region (400–600 nm) after modification of ZnO by CuO, which may be caused by the coupling band between CuO and ZnO and leads to the reduction of exciton recombination time [21].

Optical band gaps of CuO, ZnO, ZC1, ZC2 and ZC3 are estimated to be 1.70, 3.10, 2.00, 2.45 and 2.71 eV as in Fig. 6(b) from Tauc plot by $(\alpha h\nu)^{0.5} = A(h\nu\text{-}Eg)$, α and hν represents the absorption coefficient and photon energy, Eg and A represents the band gap energy and constant [22]. The results show that the band gap widths of ZC1, ZC2 and ZC3 decrease with the increase of CuO content, which is mainly due to the incorporation of Cu^{2+} ions into ZnO lattice and the formation of CuO composites [23]. The smaller bandgap of ZC indicates electrons can be more prone to transition and can produce more photogenerated carriers, which will lead to the lower resistance of sensor [21,24].

Chemical compositions and valence states of elements in ZnO, CuO and ZC2 samples were determined by XPS. Spectra of Zn 2p in Fig. 7 (a–b) show that the peaks of ZnO or ZC2 are 1021.312 eV and 1044.398 eV or 1020.714 eV and 1043.786 eV, which corresponds to spin orbit splitting of Zn $2p_{3/2}$ and Zn $2p_{1/2}$. The differences of energies of Zn $2p_{3/2}$ and Zn $2p_{1/2}$ are the same as 23.086 eV and 23.072 eV for both ZnO and ZC2, which indicates that oxidation state of Zn^{2+} exists in them [25]. Nuclear level spectra of Cu 2p in CuO and ZC2 samples are shown in Fig. 7(c–d). Peak positions of CuO or ZC2 are 933.760 eV and 953.713 eV or 932.096 eV and 952.168 eV, which corresponds to spin orbit splitting of Cu $2p_{3/2}$ and Cu $2p_{1/2}$. The differences of spin orbit splitting energies of Cu $2p_{3/2}$ and Cu $2p_{1/2}$ are also the same as 19.953 eV and 20.072 eV for both CuO and ZC2, which indicates that oxidation state of Cu^{2+} exists in them. In Fig. 7(c–d), the peaks located at 941.196 eV, 943.574 eV and 962.065 eV or 939.825 eV, 942.080 eV and 960.577 eV represent the satellite peaks of CuO, namely the accompanying peaks of Cu^{2+}, which are consistent with the peaks of CuO in other studies [26].

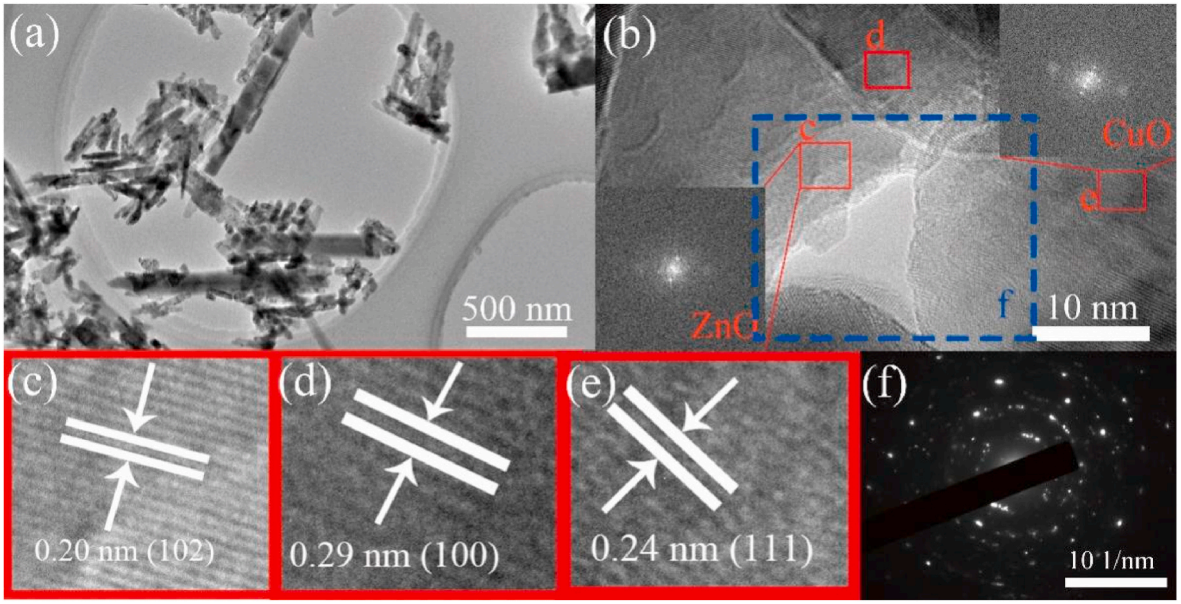

Fig. 4. (a) TEM images of ZC2, (b–e) FFT patterns and HRTEM images of ZC2, (f) SAED patterns of ZC2.

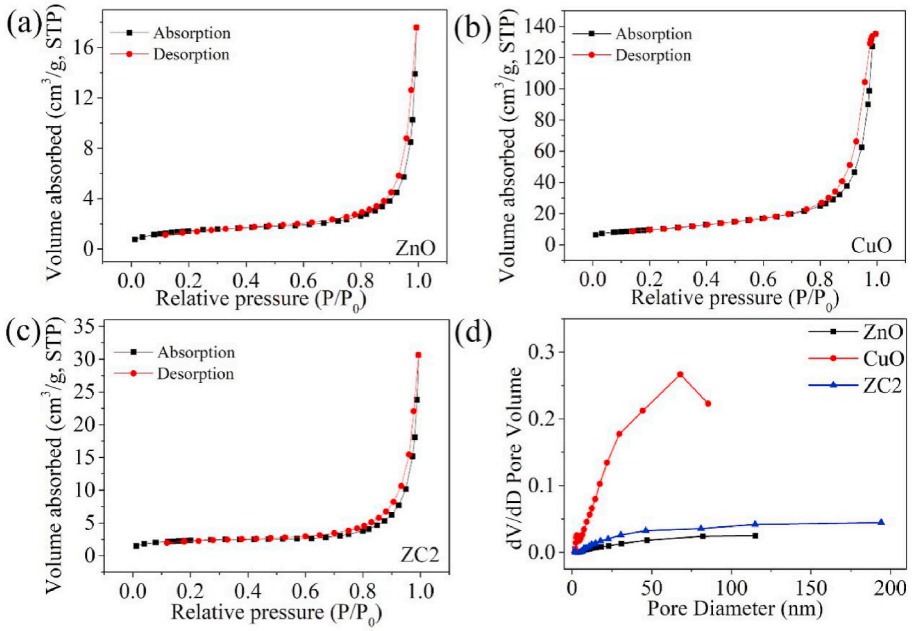

Fig. 5. N_2 adsorption-desorption isotherms of (a) ZnO, (b) CuO and (c) ZC2, (d) pore size distribution of ZnO, CuO and ZC2.

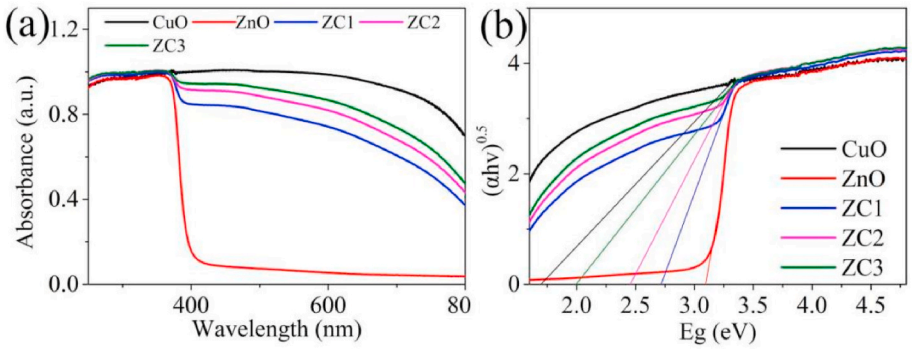

Fig. 6. (a) UV–Vis absorbance spectra, (b) Tauc plots of CuO, ZnO, ZC1, ZC2 and ZC3.

As in Fig. 7(e–g), XPS spectrum of O1s in ZnO, CuO or ZC2 sample contains O_1, O_2 and O_3 peaks, which is lattice oxygen, oxygen vacancy and oxygen free radical. Contents of O_1, O_2 and O_3 in ZnO, CuO and ZC2 samples are shown in Table 1. The increase of O_2 on surface of the material provides more active sites for the adsorption of gas molecules and can increase selectivity of the sensor for gas molecules [27]. The increase of O_3 on the material surface can provide more oxygen free radicals for the redox reaction of gas molecules, which has a significant promoting effect on gas sensitive performance of the sensor [28]. As in Table 1, O_2 content of CuO modified ZnO is increased from 21.35% of ZnO to 43.46%, and O_3 content is increased from 23.57% of ZnO to 43.10%, this may be related to the microstructure and formation of ZC heterostructure [27,28]. Contents of O_2 and O_3 in ZC2 are significantly higher than that of ZnO and CuO samples, which can provide more oxygen vacancies and oxygen free radicals for the adsorption of oxygen molecules and target gas molecules, so it is more conducive to the improvement of gas sensitivity of ZC2 sensor.

3.2. Gas sensor performance analysis

Fig. 8 shows the curves of real-time current response of ZnO, CuO, ZC1, ZC2 and ZC3 sensors to different gases under the same conditions. The comprehensive analysis shows the response of ZC2 to NH_3 is enhanced by 3 orders of magnitude compared with pure ZnO and CuO. This means that ZC2 sensor has good gas sensing response to NH_3. In addition, to further study the gas sensitivity of ZnO, CuO, ZC1, ZC2 and ZC3 sensors, CO and CO_2 performance tests were carried out, as shown in Fig. S1. This further confirms the selectivity of ZC2 to NH_3.

For more intuitively study the gas sensing performance the cylindrical analysis of its response is carried out. Fig. 9(a) is a columnar analysis of the response of ZnO, CuO and ZC2 sensors exposed to 1000 ppm NH_3, H_2O_2, HCHO, C_3H_6O and C_2H_6O gas environment. Obviously, under the same conditions, ZC2 has a higher response to NH_3 and a lower response to other gases. This not only shows that the sensor has good gas sensing performance for NH_3, but also shows that the sensor has strong single selectivity in response to NH_3. In addition, the analysis of error lines in Fig. 9(a) shows that the gas sensitive characteristics of the ZC2 sensor have good reproducibility. Fig. 9(b) is dynamic response curve of ZC2 sensor for repeatability at 1000 ppm NH_3. The average response value reaches around 5160 and there is no obvious current attenuation in three cycle tests, which has good repeatability for the sensor. The response/recovery time of sensor play an important role, which is defined as the current change of sensor reaches to 90% of the required stable value when the target gas is injected and desorbed, respectively [2]. Fig. 9(c) shows the response/recovery time (2.3 s/2.1 s) of ZC2 to 1 ppm NH_3, which means ZC2 has good response/recovery ability to NH_3.

For study influence of humidity to ZC2 sensor, we used the sensor to

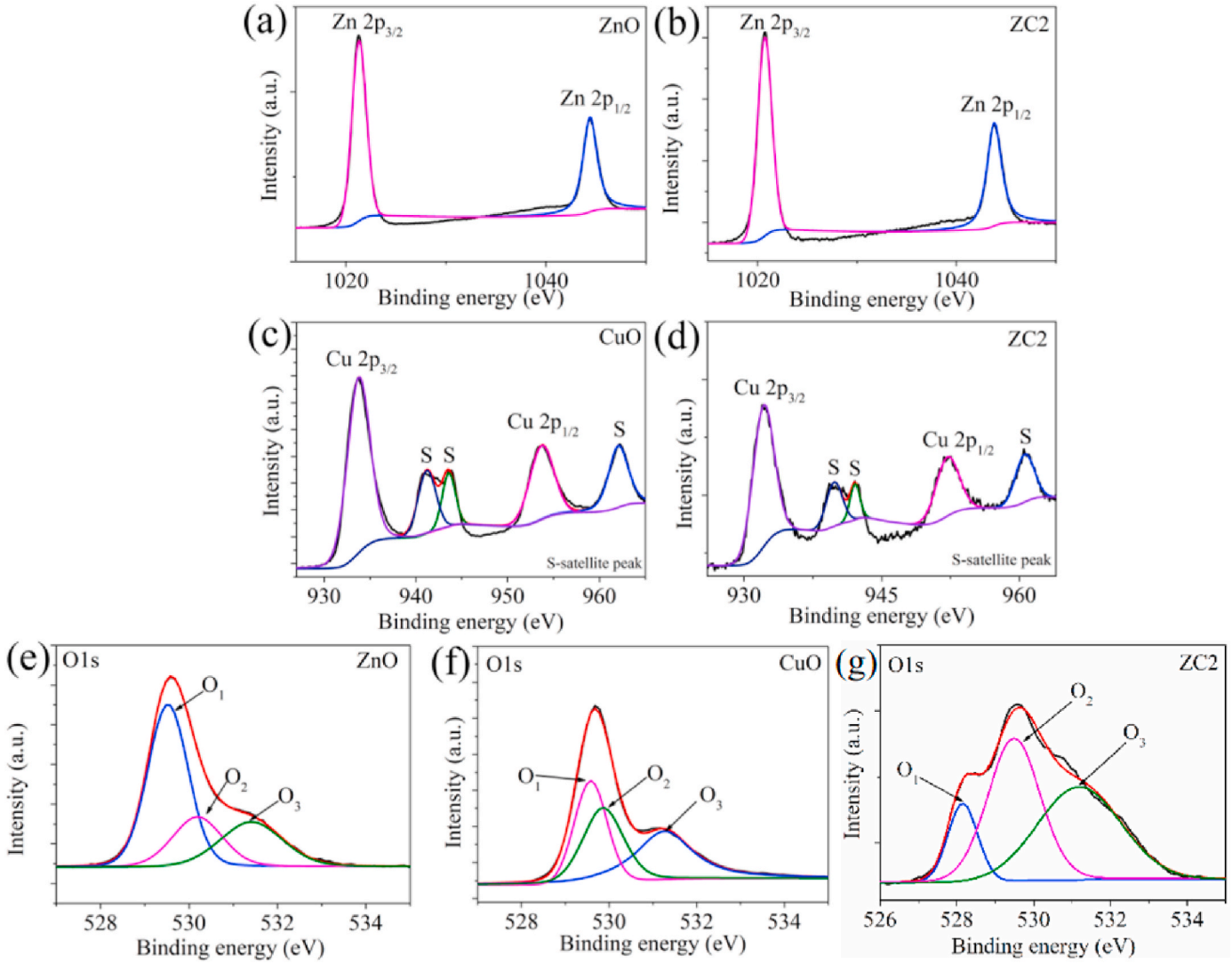

Fig. 7. (a–b) Zn XPS spectra of ZnO and ZC2, (c–d) Cu XPS spectra of CuO and ZC2, (e–g) O1s XPS spectra of ZnO, CuO and ZC2.

Table 1
Contents of O_1, O_2 and O_3 in ZnO, CuO and ZC2.

Samples	Oxygen species	Binding energy (eV)	Relative percentage (%)
ZnO	O_1	529.525	55.08%
	O_2	530.190	21.35%
	O_3	531.411	23.57%
CuO	O_1	529.575	32.13%
	O_2	529.857	31.95%
	O_3	531.263	35.92%
ZC2	O_1	528.155	13.44%
	O_2	529.488	43.46%
	O_3	531.186	43.10%

test the current change of NH_3 with a concentration of 3 ppm in different RH environments, and the response analysis can be found in Fig. 9(d). In this experiment, different RH environments were obtained as in section 2.3. As can be seen in Fig. 9(d), as the increase of humidity, making the response of sensor to NH_3 increases slightly. This is because the increase in humidity will lead to more water molecules on the test electrode, and a small number of water molecules will be ionized, resulting in an increase in the current. With reference to the detection of NH_3 with a concentration of 3 ppm in the air humidity (blue histogram), the change of response is from 17.01 to 22.67 in the 11%–85% RH, indicating that humidity has relatively little influence, which means ZC2 sensor has good humidity resistance stability. In addition, Fig. 9(e) is the actual response of the ZC2 sensor to 11%–85% RH, corresponding to the blue bar chart in Fig. 9(d), which further confirms the good moisture resistance of the ZC2 sensor.

Fig. 10(a) shows the sensitivity of ZC2 sensor to different concentrations of NH_3 at RT. Response values of it are 1.59, 7.36, 17.30, 39.00, 70.00, 131.00 and 259.00 to 1, 1.5, 3, 6, 12, 25 and 50 ppm, respectively. In Figs. 9(b) and Fig. 10(a), the sensing kinetics are different from the cases toward 1000 ppm and 1–50 ppm NH_3. It seems that quicker adsorption/desorption balance is established for low concentration case than that for high one, which is due to the high concentration of NH_3 molecules affects the progress rate of redox reaction. In Fig. 10(b), response values of ZC2 sensor to NH_3 are fitted, and linear relationship is $R = 5.1638C + 2.3728$, or the linear correlation coefficient is $R^2 = 0.9975$. The response value has a good linear relationship for NH_3 at low concentration. In addition, the error analysis in Fig. 10(b) clearly shows that the ZC2 sensor has good reproducibility. RMS and LOD of ZC2 sensor for NH_3 can be obtained from following Eqs. (1) and (2) [29,30]:

$$RMS = [\sum \frac{(N_i - N)^2}{N - 1}]^{\frac{1}{2}} \quad (1)$$

$$LOD = \frac{3 \times RMS}{Slope} \quad (2)$$

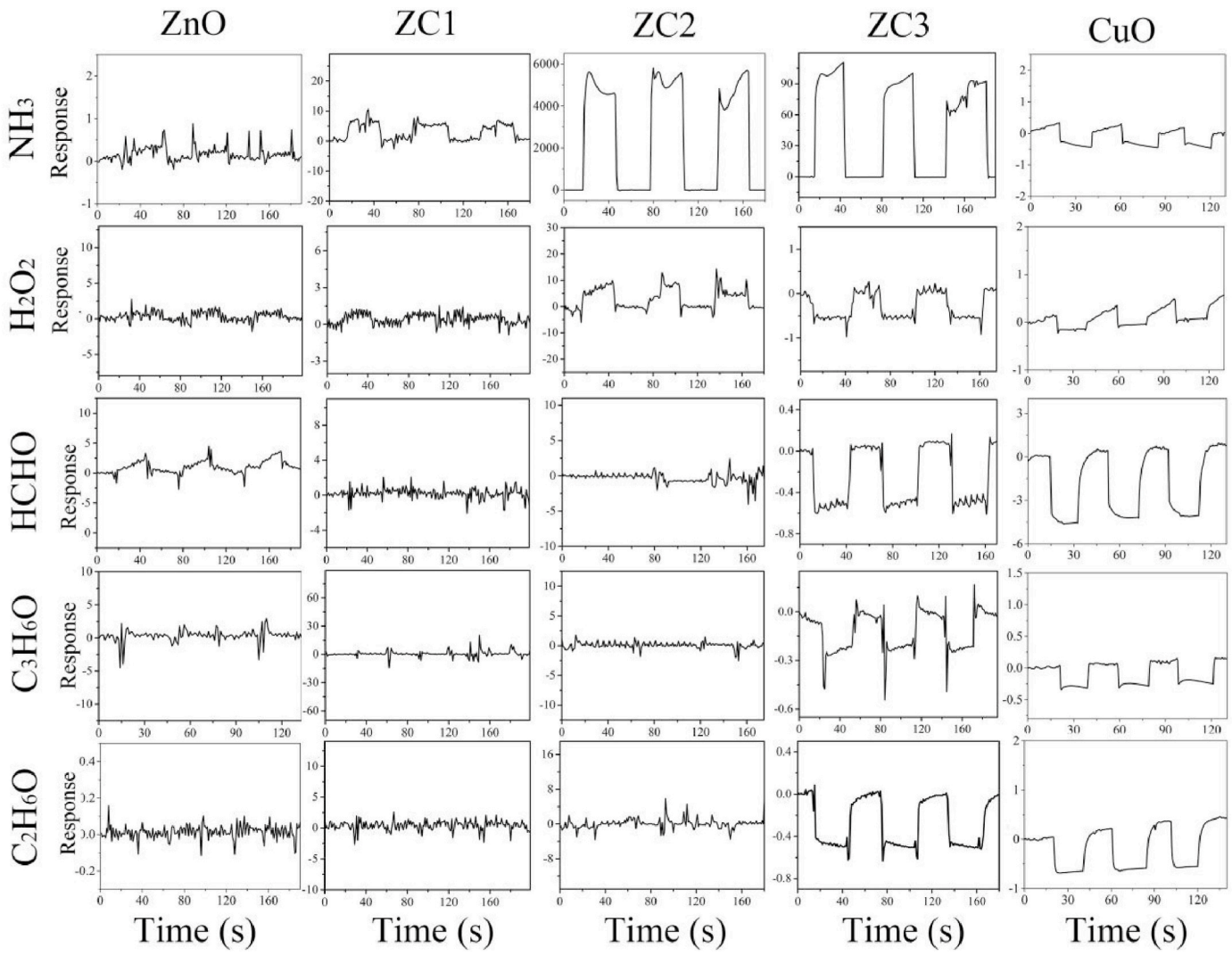

Fig. 8. Real time dynamic response curves of ZnO, ZC1, ZC2, ZC3 and CuO to different gases (NH_3, H_2O_2, HCHO, C_3H_6O and C_2H_6O) with 1000 ppm concentration at RT.

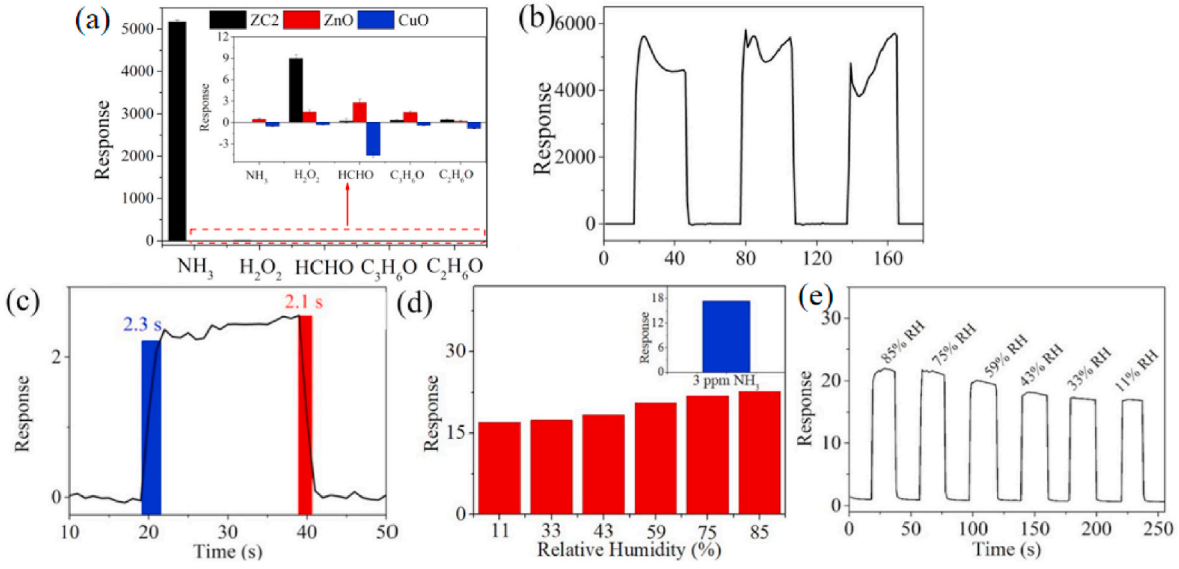

Fig. 9. (a) Histograms based on ZnO, CuO and ZC2 average response value to 1000 ppm different gases, (b) repeatability of ZC2 for 1000 ppm NH_3, (c) response/recovery time of ZC2 for 1 ppm NH_3, (d) histogram of ZC2 response to different RH at 3 ppm NH_3 and (e) real-time current response curve corresponding to (d).

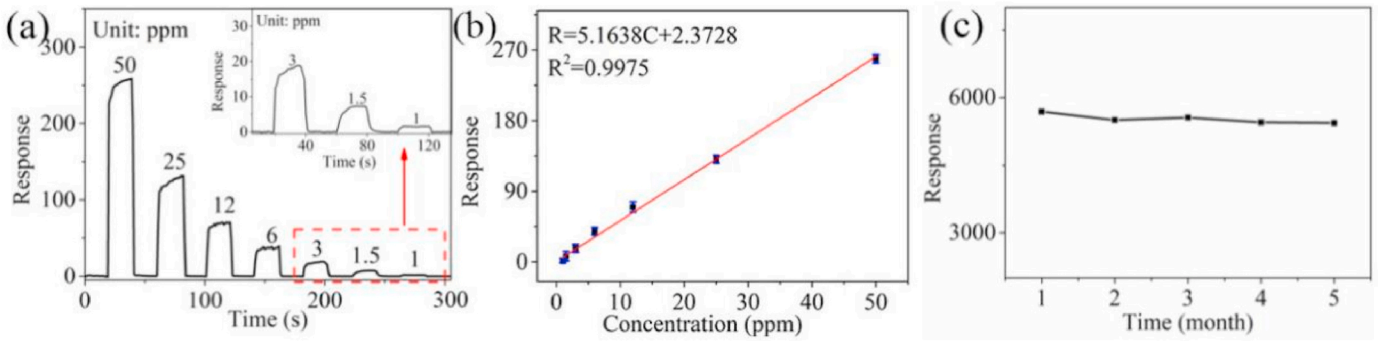

Fig. 10. (a) Response curve of ZC2 to NH_3 at different concentrations, (b) linear fitting and reproducibility of the ZC2 for 1–50 ppm NH_3 concentration and (c) long-term stability of ZC2.

where RMS is root mean square deviation of fifth-order polynomial fitting calculation, and Slope is that of the linear fitting with respect to gas concentration. On the basis of response curve, 10 data points are selected for fifth-order polynomial fitting. Calculations show that LOD of ZC2 sensor for NH_3 is 0.39 ppm. Comparisons of performance of NH_3 sensor based on CuO or ZnO composite are listed in Table 2. It is means that NH_3 sensor based on ZC heterojunction has lower detection limit and shorter response/recovery time. In Fig. 9(c), ZC2 sensor response value to 1000 ppm NH_3 changes by 4.5% in 5 months. The decrease in response value of less than 5% indicates long-term stability of ZC2 sensor, which means that the sensor has good stability.

3.3. Adsorption energy calculations

All the calculations were completed in DMOL^3 code based on density functional theory (DFT) method [32]. The generalized gradient approximation (GGA) with Perdew-Burke-Ernzerhof (PBE) approximation was employed to the exchange-correlation functional with double numeric quality basis set with polarization functions (DNP) [33,34]. All the structures are fully geometry optimized before calculations, and spin-unrestricted self-consistent field calculation was done with a convergence criterion of 2×10^{-6} a.u.. The atoms were relaxed within a force convergence criterion of 0.004 Hartree/Å (1 Hartree = 27.2 eV), the maximum displacement parameter is set to 0.005 Å, and the convergence standard in total energy was set to be 1×10^{-5} Hartree. To improve convergence, the value of smearing was set to 0.004 Hartree. In addition, the crystal structures of ZnO and CuO are hexagonal wurtzite and monoclinic respectively [34–36].

Theoretical structure models of CuO, ZnO and ZC2 are shown in Fig. 11(a–c), and theoretical adsorption models of NH_3 for CuO, ZnO and ZC2 are shown in Fig. 11(d–f). In all the models, green region is the fixed atom position invariant region, which is used to simulate internal structures of CuO, ZnO and ZC2 supercells, and supercell size of them are $5.92 \times 6.10 \times 50.00$ Å^3, $6.57 \times 10.31 \times 60.00$ Å^3 and $6.57 \times 10.31 \times 60.00$ Å^3, respectively. In order to verify NH_3 adsorption capacity of CuO, ZnO and ZC2 to NH_3, adsorption energy and adsorption distance were calculated by first principles. Adsorption energy (E_{ads}) is defined as $E_{ads} = - E_{S + NH3} + E_S + E_{NH3}$. In this formula, $E_{S + NH3}$, E_s and E_{NH3} represent total energy of adsorption system, energy of the sample and gas molecule, respectively.

Table 3 shows calculation results. Adsorption energies of CuO, ZnO and ZC2 to NH_3 corresponding to the adsorption model in Fig. 11(d–f), are 1.10 eV, 1.56 eV and 1.76 eV, respectively. Results show that ZC2 has the largest binding energy and the strongest adsorption capacity for NH_3 molecules. Compared with adsorption systems of CuO and ZnO for NH_3, ZC2 for NH_3 is the most stable [32,34]. In addition, the above conclusions also indicate that the sensitivity of ZC2 for NH_3 molecule is higher than that of CuO and ZnO, which is consistent with the above experimental results [37].

In order to further verify stability of ZC2 adsorption system, net charges of NH_3 molecules in different adsorption systems and polarization degree of NH_3 molecules were analyzed. In Table 4, corresponding net charges of NH_3 in CuO, ZnO and ZC2 adsorption systems are 0.224, 0.180 and 0.276, respectively. Charges of N, H_1, H_2 and H_3 atoms in adsorbed NH_3 molecules on ZC2 heterojunction are −0.505, 0.265, 0.222 and 0.294, respectively. Compared with the charges of NH_3 molecules in CuO and ZnO adsorption systems, the net charge of NH_3 molecules adsorbed on ZC2 heterojunction is the largest and the polarity is the strongest [32–37]. This is due to the existence of heterojunction in ZC2 adsorption system, which enhances thickness of ZC2 electron depletion layer and forms a strong build-in electric field. Therefore, NH_3 molecules will be adsorbed on surface of ZC2 heterojunction in large quantities, and redox reaction will take place with free oxygen and NH_3 molecules. The redox reaction releases a large number of free electrons into ZC2 heterojunction, resulting in a decrease of thickness of electron depletion layer at the heterojunction. Change of the thickness of depletion layer leads to a sharp decrease in resistance, which obviously shows that response value of ZC2 sensor to NH_3 gas changes by three major orders of magnitude [13,15,32].

In Fig. 11(d–f), adsorption distances of Cu–N, Zn–N and Cu–N are 2.050 Å, 2.092 Å and 2.035 Å when NH_3 molecules are adsorbed on Cu, Zn and Cu atoms of CuO, ZnO and ZC2 samples, respectively. Adsorption distance of Cu atom in ZC2 is the shortest and adsorption structure is the most stable, so adsorption energy for ZC2 to NH_3 molecule is the highest [38,39].

Table 2
Results of this study compared with those reported NH_3 sensors.

Materials	Temperature (°C)	Detect Concentration (ppm)	Response/Recovery time (s)	Detection limit	References
ZnO-MWCNT	RT	10	13.687/107.109	–	[1]
Al–ZnO/CuO	RT	500	14/9	50 ppm	[2]
PVP/CuO 8 wt%	RT	200	17/15	100 ppm	[3]
3D printed CuO	RT	25	75/25	–	[22]
NiO@CuO	RT	100	72.5/35	46.5 ppb	[30]
CuO/CuS@NSC	RT	100	24/22	1 ppm	[31]
CuO/ZnO	RT	1	2.3/2.1	0.39 ppm	This work

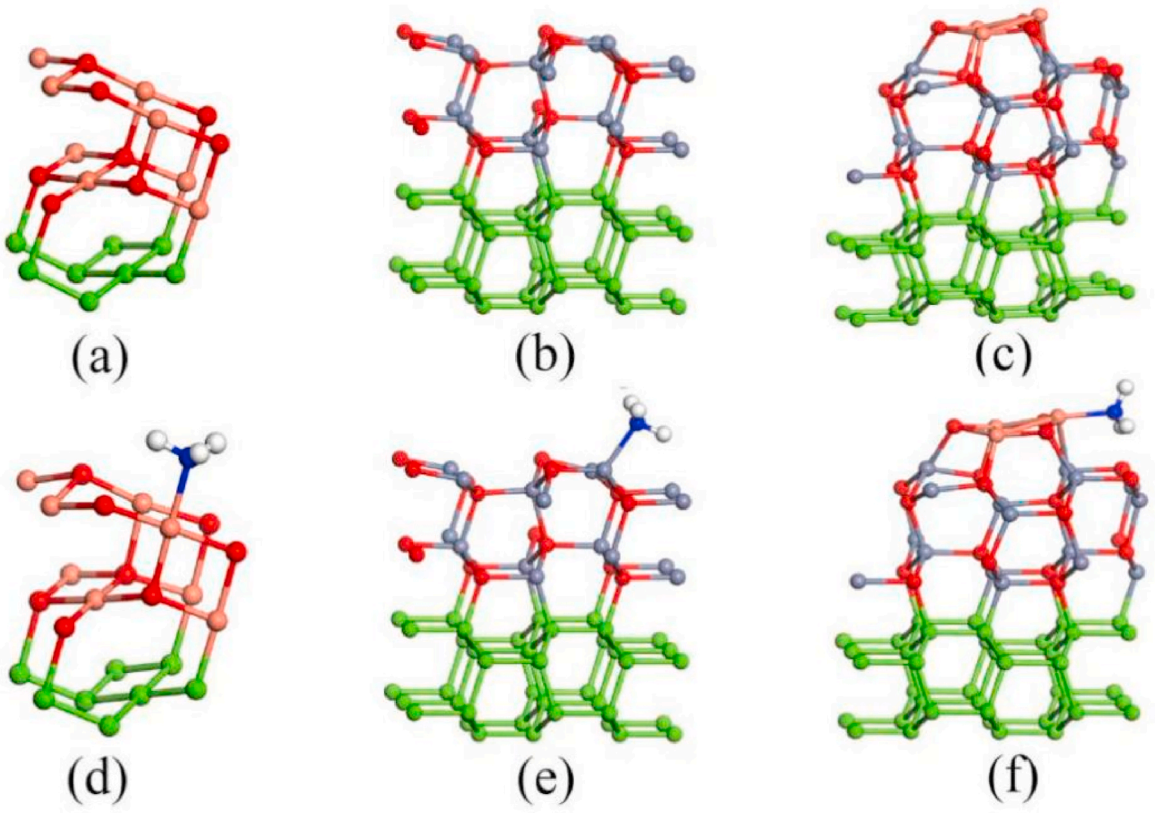

Fig. 11. Optimized adsorption structure models for CuO, ZnO and ZC2 without and with gas molecules. (a–c) Theoretical structure models of CuO, ZnO and ZC2 without gas molecule adsorption, (d–f) adsorption structure model of CuO, ZnO and ZC2 with NH_3 molecules. (white –H, blue –N, red –O, pink -Cu and gray -Zn). (For interpretation of the references to color in this figure legend, the reader is referred to the Web version of this article.)

Table 3
Adsorption energy of CuO, ZnO and ZC2 for NH3.

Adsorption model	CuO–NH_3	ZnO–NH_3	ZC2-NH_3
E_{ads}(eV)	1.10	1.56	1.76

Table 4
Amount of charges (Unit: 1.6×10^{-19} C) corresponding to N, H_1, H_2 and H_3 atoms of NH_3 molecule in CuO, ZnO and ZC2 adsorbed systems.

Adsorption model	CuO–NH_3	ZnO–NH_3	ZC2-NH_3
N	−0.456	−0.557	−0.505
H_1	0.222	0.219	0.265
H_2	0.218	0.220	0.222
H_3	0.240	0.298	0.294
Net charge	0.224	0.180	0.276

3.4. Sensing mechanism

In order to evaluate the interaction of NH_3 molecules on ZC heterojunction surface and the change of their electronic properties, band structure analysis was carried out. In Fig. 12, energy band diagram of ZC heterojunction is shown. Since the different band gaps between CuO and ZnO, electrons in ZnO and holes in CuO diffuse in the opposite direction until the system reaches equilibrium at Fermi level [40–42]. Therefore, a p-n heterojunction is formed at the interface between two different metal oxide semiconductor, which can expand the electron depletion layer, and the separation of electron/hole carriers increases the number of oxygen free radicals. Additionally, the gas sensing mechanism of heterojunction sensors composed of metal oxide semiconductors is generally surface control type [2]. It is explained that redox reaction between target gas and surface free oxygen radicals causes the change of depletion layer thickness at heterojunction, and then the resistance changes. The mechanism is divided into adsorption process, redox reaction process and desorption process [2,25]. The action mechanism of ZC heterojunction gas sensor on NH_3 molecule is analyzed as follows:

(1) Oxygen molecules in the air mainly capture electrons at E_{c1} on ZC surface to generate a large number of oxygen free radicals ($O_{2(air)} + e^- \rightarrow O_2^-{}_{(gas)}$). The decrease in the number of electrons at E_{c1} causes electrons at E_{c2} to flow to E_{c1}, while holes flow in the opposite direction [2]. Therefore, the thickness of ZC heterojunction electron depletion layer increases, which is specifically reflected in the high resistance of ZC sensor under air conditions, as shown in Fig. 12(a).
(2) A mass of NH_3 molecules are adsorbed on the sensor surface under the action of built-in electric field formed by ZC heterojunction when ZC sensor is exposed to NH_3. NH_3 molecule redox reaction with oxygen free radicals on surface releases a lot of electrons to ZC heterojunction, which increases free electron number at E_{c2} in ZnO and hole number at E_{v1} in CuO, then reduce the thickness of electron depletion layer at ZC heterojunction, as shown in Fig. 12(b). This process will cause a sharp decrease in the resistance value of ZC and an increase in the current value [15,20,37].
(3) When ZC sensor is separated from NH_3 environment, a large number of oxygen molecules in the air are adsorbed on ZC surface again to capture electrons. The decrease of electrons on ZC surface will increase the thickness of depletion layer. Moreover, resistivity at heterojunction decreases and resistance value increases [2,24].

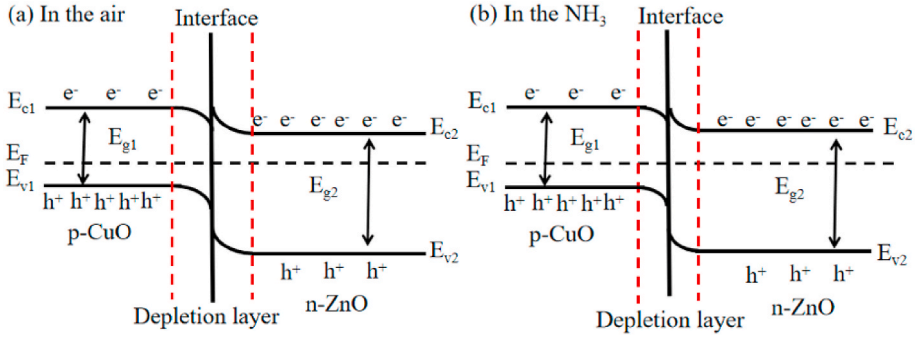

Fig. 12. ZC heterojunction energy band diagram (a) in the air and (b) in the NH_3.

4. Conclusions

An NH_3 sensor based on ZC heterojunction with high performance was prepared by hydrothermal method. Experiments show that ZC2 achieves an average response value of 5160 for NH_3 at 1000 ppm, the response/recovery time is 2.3 s/2.1 s for NH_3 at 1 ppm, which is the faster response/recovery time in the reported NH_3 gas sensors with ppm levels. Moreover, ZC2 has a good linear response to NH_3 in the range of 1–50 ppm and detection limit is 0.39 ppm. First principles calculations show that the excellent performance of ZC2 to NH_3 detection is mainly due to strong adsorption energy of ZC2 heterojunction for NH_3 molecules, and polarity of NH_3 molecules is enhanced under the action of built-in electric field formed by ZC heterojunction. Therefore, the sensor is immersed in target gas environment, a mass of NH_3 molecules are adsorbed on surface of ZC and redox reaction with oxygen radicals improves the detection performance of ZC sensor for NH_3. With simple preparation and excellent performance, such a ZC heterojunction sensor has a strong practicability for NH_3 detection at RT.

CRediT authorship contribution statement

Cao Cheng: Writing – original draft, Methodology, Investigation, Data curation, Writing – review & editing. **Chu Chen:** Validation, Software, Supervision. **Hongyan Zhang:** Resources, Supervision, Conceptualization, Formal analysis, Funding acquisition, Investigation, Methodology, Writing – review & editing. **Yong Zhang:** Supervision, Formal analysis.

Declaration of competing interest

The authors declare that they have no known competing financial interests or personal relationships that could have appeared to influence the work reported in this paper.

Acknowledgements

We acknowledge the financial support from the National Natural Science Foundation of China (No. 62064011) and Xinjiang University Ph. D. Starup Fund (No. BS150219). YZ acknowledge support of Bissell Distinguished Professorship at UNC-Charlotte.

Appendix A. Supplementary data

Supplementary data to this article can be found online at https://doi.org/10.1016/j.mssp.2022.106700.

References

[1] L. Vatandoust, A. Habibi, H. Naghshara, S.M. Aref, Fabrication of ZnO-MWCNT nanocomposite sensor and investigation of its ammonia gas sensing properties at room temperature, Synth. Met. 273 (2021) 116710.
[2] M. Poloju, N. Jayababu, M.V.R. Reddy, Improved gas sensing performance of Al doped ZnO/CuO nanocomposite based ammonia gas sensor, Mater. Sci. Eng., B 227 (2018) 61–67.
[3] H.U. Khana, M. Tariqa, M. Shahb, M. Iqbalc, M.T. Jan, Inquest of highly sensitive, selective and stable ammonia (NH_3) gas sensor: structural, morphological and gas sensing properties of polyvinylpyrrolidone (PVP)/CuO nanocomposite, Synth. Met. 268 (2020) 116482.
[4] M. Senapati, P.P. Sahu, Meat quality assessment using Au patch electrode Ag-SnO_2/SiO_2/Si MIS capacitive gas sensor at room temperature, Food Chem. 324 (2020) 126893.
[5] N.L.L. Hekiem, A.A.M. Ralib, M.A.M. Hattar, F.B. Ahmad, A.N. Nordin, R.A. Rahim, N.F. Za'bah, Advanced vapour sensing materials: existing and latent to acoustic wave sensors for VOCs detection as the potential exhaled breath biomarkers for lung cancer, Sensor Actuat. A Phys. 329 (2021) 112792.
[6] K. Liu, C. Zhang, Volatile organic compounds gas sensor based on quartz crystal microbalance for fruit freshness detection: a review, Food Chem. 334 (2021) 127615.
[7] S.M. Majhi, A. Mirzaei, H.W. Kim, S.S. Kim, T.W. Kim, Recent advances in energy-saving chemiresistive gas sensors: a review, Nano Energy 79 (2021) 105369.
[8] Y. Zhou, Y.J. Wang, Y.H. Wang, X. Li, Y.C. Guo, The impact of carrier gas on room-temperature trace nitrogen dioxide sensing of ZnO nanowire-integrated film under UV illumination, Ceram. Int. (2020).
[9] Y.J. Wang, Y. Zhou, H. Ren, Y.H. Wang, X.Y. Zhu, Y.C. Guo, X. Li, Room-temperature and humidity-resistant trace nitrogen dioxide sensing of few-layer black phosphorus nanosheet by incorporating zinc oxide nanowire, Anal. Chem. (2020).
[10] J.J. Liu, L.Y. Zhang, J.J. Fan, B.C. Zhu, J.G. Yu, Triethylamine gas sensor based on Pt-functionalized hierarchical ZnO microspheres, Sensor. Actuator. B Chem. 331 (2021) 129425.
[11] C. Feng, F. Wen, Z.H. Ying, L.L. Li, X.L. Zheng, P. Zheng, G.F. Wang, Polypeptide-assisted hydrothermal synthesis of ZnO for room temperature NO_2 gas sensor under UV illumination, Chem. Phys. Lett. 754 (2020) 137745.
[12] G.D. Li, H. Zhang, L.X. Meng, Z. Sun, Z. Chen, X.Y. Huang, Y. Qin, Adjustment of oxygen vacancy states in ZnO and its application in ppb-level NO_2 gas sensor, Sci. Bull. 65 (2020) 1650–1658.
[13] X. Liang, J. Zhang, L.Y. Du, M.Z. Zhang, Effect of resonant tunneling modulation on ZnO/In_2O_3 heterojunction nanocomposite in efficient detection of NO_2 gas at room temperature, Sensor. Actuator. B Chem. 329 (2021) 129230.
[14] R.N. Mariammal, K. Ramachandran, Study on gas sensing mechanism in p-CuO/n-ZnO heterojunction sensor, Mater. Res. Bull. 100 (2018) 420–428.
[15] S. Sharma, A. Kumar, N. Singh, D. Kaur, Excellent room temperature ammonia gas sensing properties of n-MoS_2/p-CuO heterojunction nanoworms, Sensor. Actuator. B Chem. 275 (2018) 499–507.
[16] Y. Hu, X. Zhou, Q. Han, Q. Cao, Y. Huang, Sensing properties of CuO-ZnO heterojunction gas sensors, Mater. Sci. Eng. B 99 (2003) 41–43.
[17] M.R. Yu, G. Suyambrakasam, R.J. Wu, M. Chavali, Performance evaluation of ZnO–CuO hetero junction solid state room temperature ethanol sensor, Mater. Res. Bull. 47 (2012) 1713–1718.
[18] S. Cao, Z.F. Wu, Q.H. Sun, W.Y. Zhang, S. Beysen, S.Y. Wang, T. Shaymurat, M. Zhang, H.M. Duan, Gas sensing properties of cotton-based carbon fibers and ZnO/carbon fibers regulated by changing carbonization temperatures, Sensor. Actuator. B Chem. 337 (2021) 129818.
[19] L.L. Sui, T.T. Yu, D. Zhao, X.L. Cheng, X.F. Zhang, P. Wang, Y.M. Xu, S. Gao, H. Zhao, Y. Gao, L.H. Huo, In situ deposited hierarchical CuO/NiO nanowall arrays film sensor with enhanced gas sensing performance to H_2S, J. Hazard Mater. 385 (2020) 121570.
[20] M. He, L.L. Xie, X.L. Zhao, X.B. Hu, S.H. Li, Z.G. Zhu, Highly sensitive and selective H_2S gas sensors based on flower-like WO_3/CuO composites operating at low/room temperature, J. Alloys Compd. 788 (2019) 36–43.
[21] S. Prathap Selvaraj, Enhanced surface morphology of copper oxide (CuO) nanoparticles and its antibacterial activities, Mater. Today Proc. (2020).
[22] G. Chaloeipote, R. Prathumwan, K. Subannajui, A. Wisitsoraat, C. Wongchoosuk, 3D printed CuO semiconducting gas sensor for ammonia detection at room temperature, Mater. Sci. Semicond. Process. 123 (2021) 105546.
[23] J.E. Morales-Mendoza, F. Paraguay-Delgado, Widening UV–Vis absorption band by Cu doped ZnO and ZnO/CuO composite, Mater. Lett. 291 (2021) 129494.

[24] R.R. Kumar, T. Murugesan, A. Dash, C.H. Hsu, S. Gupta, A. Manikandan, A. K. Anbalagan, C.H. Leec, N.H. Taia, Y.L. Chueh, H.N. Lin, Ultrasensitive and light-activated NO_2 gas sensor based on networked MoS_2/ZnO nanohybrid with adsorption/desorption kinetics study, Appl. Surf. Sci. 536 (2021) 147933.
[25] X. Wang, S.h. Li, L.l. Xie, X. Li, D.H. Lin, Z.G. Zhu, Low-temperature and highly sensitivity H_2S gas sensor based on ZnO/CuO composite derived from bimetal metal-organic frameworks, Ceram. Int. 46 (2020) 15858–15866.
[26] Q. Hu, W.J. Zhang, X.Y. Wang, Q. Wang, B.Y. Huang, Y. Li, X.H. Hua, G. Liu, B. S. Li, J.Y. Zhou, E.Q. Xie, Z.X. Zhang, Binder-free CuO nanoneedle arrays based tube-type sensor for H_2S gas sensing, Sensor. Actuator. B Chem. 326 (2021) 128993.
[27] H. Bai, H. Guo, J. Wang, Y. Dong, B. Liu, Z.L. Xie, F.Q. Guo, D.J. Chen, R. Zhang, Y. D. Zheng, A room-temperature NO_2 gas sensor based on CuO nanoflakes modified with rGO nanosheets, Sensor. Actuator. B Chem. 337 (2021) 129783.
[28] R.N. Mariammal, K. Ramachandran, Study on gas sensing mechanism in p-CuO/n-ZnO heterojunction sensor, Mater. Res. Bull. 100 (2018) 420–428.
[29] H.Y. Xu, J.D.X. Ju, W.R. Li, J. Zhang, J.Q. Wang, B.Q. Cao, Superior triethylamine-sensing properties based on TiO_2/SnO_2 n–n heterojunction nanosheets directly grown on ceramic tubes, Sensor. Actuator. B 228 (2016) 634–642.
[30] Y.L. Zhou, J. Wang, X.K. Li, Flexible room-temperature gas sensor based on poly (para-phenylene terephthalamide) fibers substrate coupled with composite NiO@ CuO sensing materials for ammonia detection, Ceram. Int. 46 (2020) 13827–13834.
[31] T. Ahamad, M. Naushad, S.M. Alshheri, Fabrication of highly porous N/S doped carbon embedded with CuO/CuS nanoparticles for NH_3 gas sensing, Mater. Lett. 268 (2020) 127515.
[32] Y.L. Yong, Q.X. Zhou, X.Y. Su, Y.M. Kuang, C.R.A. Catlow, X.H. Li, Hydrogenated $Si_{12}Au_{20}$ cluster as a molecular sensor with high performance for NH_3 and NO detection: a first-principle study, J. Mol. Liq. 289 (2019) 111153.
[33] C.H. Zheng, H.B. Zhao, The microscopic oxidation mechanism of NH_3 on CuO (111): a first-principles study, Fuel Process. Technol. 213 (2021) 106712.
[34] P. Srivastava, Abhishek, N.K. Jaiswal, First-principles investigation of CO_2 and NH_3 adsorption on antimonene nanoribbons, Mater. Today Proc. 28 (2020) 65–69.
[35] F. Safari, M. Moradinasab, M. Fathipour, H. Kosina, Adsorption of the NH_3, NO, NO_2, CO_2, and CO gas molecules on blue: a first-principles study, Appl. Surf. Sci. 464 (2019) 153–161.
[36] S.M. Aghaei, M.M. Monshi, I. Torres, S.M.J. Zeidi, I. Calizo, DFT study of adsorption behavior of NO, CO, NO_2, and NH_3 molecules on graphene-like BC_3: a search for highly sensitive molecular sensor, Appl. Surf. Sci. 427 (2018) 326–333.
[37] S. Singh, J. Deb, U. Sarkar, S. Sharma, $MoSe_2$ crystalline nanosheets for room-temperature ammonia sensing, ACS Appl. Nano Mater. 3 (2020) 9375–9384.
[38] N.L.L. Hekiem, A.A.M. Ralib, M.A.M. Hattar, F.B. Ahmad, A.N. Nordin, R.A. Rahim, N.F. Za'bah, Advanced vapour sensing materials: existing and latent to acoustic wave sensors for VOCs detection as the potential exhaled breath biomarkers for lung cancer, Sensors Actuat. A Phys. 329 (2021) 112792.
[39] X. Gao, Q. Zhou, J.X. Wang, L.N. Xu, W. Zeng, Adsorption of SO_2 molecule on Ni-doped and Pd-doped graphene based on first-principle study, Appl. Surf. Sci. 517 (2020) 146180.
[40] Y. Zhou, C. Gao, Y.C. Guo, UV assisted ultrasensitive trace NO_2 gas sensing based on few-layer MoS_2 nanosheet-ZnO nanowire heterojunctions at room temperature, J. Mater. Chem. (2018).
[41] S. Singh, J. Deb, U. Sarkar, S. Sharma, MoS_2/WO_3 nanosheets for detection of ammonia, ACS Appl. Nano Mater. 4 (2021) 2594–2605.
[42] S. Singh, J. Deb, U. Sarkar, S. Sharma, MoS_2/MoO_3 nanocomposite for selective NH_3 detection in a humid environment, ACS Sustain. Chem. Eng. 9 (2021) 7328–7340.